Journal of Materials Chemistry A

Accepted Manuscript

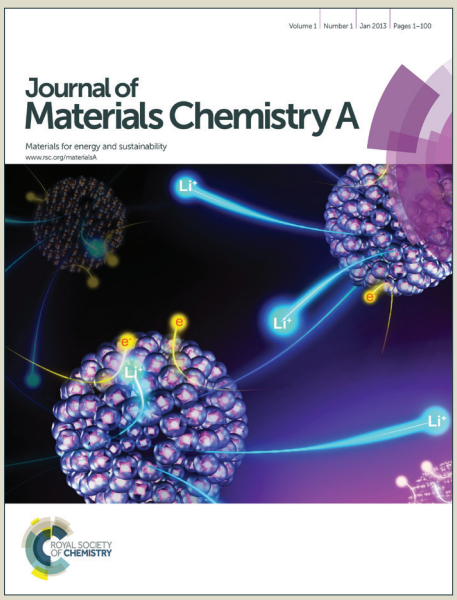

ROYAL SOCIETY OF CHEMISTRY

www.rsc.org/materialsA

Journal Name

RSCPublishing

ARTICLE

Comprehensive Study of Medium-Bandgap Conjugated Polymer Merging a Fluorinated Quinoxaline with Branched Side Chains for High-Efficient and Air-Stable Polymer Solar Cells

Cite this: DOI: 10.1039/x0xx00000x

Received 00th January 2012,
Accepted 00th January 2012

DOI: 10.1039/x0xx00000x

www.rsc.org/

Wei-Hsuan Tseng,[bc] Hsieh-Chih Chen,*[ac] Yun-Chen Chien,[a] Chi-Chang Liu,[a] Yung-Kang Peng,[a] Yu-Sin Wu,[a] Jung-Hung Chang,[b] Shih-Hung Liu,[a] Shang-Wei Chou,[a] Chien-Liang Liu,[a] Ying-Hsiao Chen,[a] Chih-I Wu,*[bc] and Pi-Tai Chou,*[ac]

A new medium-bandgap conjugated copolymers comprising a rigidly fused benzo[1,2-b:4,5-*b'*]-dithiophene (BDT) unit and a fluorinated quinoxaline moiety through a thiophene π-spacer has been rationally designed and synthesized by Stille coupling polymerization and thoroughly evaluated for use as a donor material in bulk-heterojunction polymer solar cells (BHJ PSCs). A comprehensive study of the structure-function relationship in the PSCs was also explored. The PDBTQEH copolymer exhibits good solubility in a wide range of organic solvents and has a high hole mobility. Introduction of highly electronegative fluorine atoms to quinoxaline moiety further lowers both the highest occupied molecular orbital (HOMO) and the lowest unoccupied molecular orbital (LUMO) energy levels of polymer, which is beneficial for attaining higher open-circuit voltage (V_{oc}) and long-term stability. Conventional architecture BHJ PSCs using PBDTQEH:$PC_{71}BM$ (1:1, *w*/*w*) displays a high power conversion efficiency (PCE) of 5.90%. Compared with the same composition, device in the inverted configuration reveals a rather high PCE of 6.36% with a V_{oc} of 0.78 V, a short-circuit current density (J_{sc}) of 12.72 mA cm^{-2}, and a high fill factor (FF) of 64.3%. The inverted device also demonstrates outstanding air stability; without any encapsulation, the solar efficiency of the device remains above 74% of the original value after storage in air for 1000 h.

Introduction

Polymer solar cells (PSCs) incorporating abundant advantages of low cost, lightweight, solution processability, and mechanical flexibility have triggered the exploration of new niches and positioned the relevant technology on the cusp of genuine impact in the clean and renewable energy marketplace.[1] Nowadays, the most successful device structure for high performance PSCs is based on the bulk-heterojunction (BHJ) concept, which involves a three-dimensional interpenetrating network of conjugated polymers blended with soluble fullerene derivatives[2-15] or nanocrystals[16-20] to ensure maximum internal interfacial area for efficient charge separation. Among various donors used in BHJ solar cells, the most promising ones are conjugated in-chain donor-acceptor (D-A) alternating copolymers, which consist of alternating D and A blocks in each repeating unit. This configuration plays an important role in designing high-performance PSCs due to the intramolecular electrostatic attraction, arising from the electron density asymmetry along the conjugated backbone. Therefore, the D-A strategy not only allows effective tuning of the bandgap, but also tailoring of the frontier molecular orbital energies of the resultant polymer.[21] To achieve high efficiency of PSCs, the electron-donating conjugated polymers need to have sufficient solubility for solution processability and possess appropriate bandgaps to harvest more solar flux to maximize the short-circuit current density (J_{sc}), high hole mobility for efficient charge transport, and suitable highest occupied molecular orbital (HOMO) energy levels to promote high open-circuit voltage (V_{oc}). Furthermore, exciton dissociation and photogeneration at the interfaces of the bicontinuous networks result in the formation of heteromolecular charge transfer states with the hole occupying in the polymer phase and the electron residing in the fullerene phase of the heterojunction.[22-29] The produced charge carriers are then available for extraction at the device electrodes to an external circuit. As a result, through the invention of novel low or medium bandgap polymers, efficient extraction of charge carriers, and better control over the nanoscale morphologies of interpenetrating electron D-A networks have given rise to power conversion efficiencies (PCEs) in the level of > 8%.[30-34]

However, the stability and degradation issues are still the primary obstructions for commercialization of PSCs. Therefore, further improvements in PCE and long-term air stability are the major challenges before commercial applications. In general, a conventional BHJ PSC applies indium-doped tin oxide (ITO) as a transparent anode, and a low work-function metal such as Al is used as a cathode. However, these conventional PSCs display low environmental stability owing to the highly oxidative cathodes.[35,36] Furthermore, the hole-transporting buffer layer of poly(3,4-ethylenedioxythiophene): poly(styrenesulfonic acid) (PEDOT:PSS)

is acidic enough to gradually etch the ITO anode,[37,38] restricting the device stability. In order to overcome these drawbacks, inverted device architecture has been addressed as an alternate strategy for raising the stability of PSCs. In inverted PSCs, electrons are collected through an electron-transporting buffer layers (e.g. ZnO and TiO_2) deposited on ITO, and high work-function metals such as Au and Ag collect the holes.

Among the various donor moieties used in D-A copolymer photovoltaic materials, benzo[1,2-*b*:4,5-*b′*]-dithiophene (BDT) is currently one of the most favorite donor unit due to its excellent electron-donating property, rigid coplanar structure by fusing a benzene with two flanking thiophene units, high hole mobility, extremely extended π-conjugated structures, and proper side chain patterns for enhanced solubility.[39,40] The introduction of this planar and rigid unit lowers energetic disorder through stiffening of the backbone and promotes close intermolecular π-stacking, which aids the formation of highly ordered domains.[41] Very recently, we have reported a certified high-efficiency PSCs upon BDT-fluorinated quinoxaline-based copolymer (PBDT-TFQ) with linear alkoxy substituted side-chains.[31] However, PBDT-TFQ did not exhibit satisfactory long-term air-stability in the inverted device architecture. The reason may be attributed to the unstable morphology of the blends (vide infra). The morphology of the aggregates was determined by the free energy competition between the interfacial energy associated with unfavorable interactions (between the rigid backbone and side-chain domains) and the free-volume entropy associated with side chains.[5] In this regard, we therefore made great efforts to replace linear alkoxy substituted side-chains with branched alkoxy ones to form more stable morphology owing to the fact that the entropic factor becomes dominant, and the interfacial energy must be sacrificed to provide more free volume.[5] In this context, a new fluorinated quinoxline-based D-A copolymer with medium bandgap, namely, poly{4,8-bis(2'-ethylhexyloxy)-benzo[1,2-*b*:4,5-*b′*]dithiophene-alt-[5,8-bis(5'-thiophen-2'-yl)-6,7-difluoro-2,3-bis(3"-(2-ethylhexyl)oxyphenyl)quinoxaline]} (PBDTQEH, see **Scheme 1**), was thus designed and synthesized. To our knowledge, the synthesis and application of PBDTQEH copolymer in BHJ solar cells has not yet been reported. The solubility of PBDTQEH was successfully enhanced with branched side chain on quinoxaline moiety, which gave rise to higher number average molecular weight (M_n) to be 57.8 kg mol^{-1}. More encouragingly, the introduction of fluorine atoms with high electron affinity nature to the quinoxaline moiety is effective in further improving the long-term stability of PSC by lowering both HOMO and LUMO energy levels of polymer.[3,11,31] Additionally, in an inverted device configuration, we systematically examine the electrical properties of ZnO buffer layer by varying the layer counts of ZnO and successfully improve PCEs from 5.42% to 6.36% while using 5-layers of ZnO films. The device also demonstrates a superior stability, the PCE of the inverted device remains above 74% of the original solar efficiency even after storage in air for 1000 h without any encapsulation.

Experimental

Measurement and Characterization.

Detailed experimental procedures for the synthesis and characterization of the PBDTQEH copolymer are given in the Supporting Information. All NMR spectra were recorded on a Varian Mercury 400. Mass spectra were obtained on a FINNIGAN LCQ mass spectrometer. Chemical shifts (δ), quoted in parts per million (ppm), and coupling constants (J) were recorded in Hertz (Hz). All NMR spectra were recorded in deuterated chloroform or 1,1,2,2-tetrachloroethane ($CDCl_3$ or $C_2D_2Cl_4$) and solvent containing 0.003% TMS as an internal reference. The molecular weight and molecular weight distribution of the synthesized polymers were measured with a Waters GPC (Breeze system) using tetrahydofuran (THF) as an eluent at 35 °C. The apparatus was equipped with two Waters Styragel columns (HR3 and HR4E), a refractive index detector (Waters 2414), and a dual-wavelength absorbance detector (Waters 2487). Polystyrene standards (Waters) were used for calibration. The absorption spectra were recorded on a Hitachi U-4100 spectrophotometer. Photoluminescence spectra were obtained with a double monochromator fluorometer (Jobin-Yvon) equipped with a Peltier and a water cooled detectors sensitive in the NIR spectral range down to 0.8 eV. Photoemission experiments were carried out by ultraviolet photoemission spectroscopy (UPS) and inverse photoemission spectroscopy (IPES) in an ultra high vacuum (UHV) chamber with a base pressure of 1×10^{-9} Torr. The photon energies of UPS are 21.2 eV (He I) with an experiment resolution of 0.15 eV. IPES was carried out in the isochromat mode to diminish the beam-reduced damage with a resolution of around 0.45 eV.[52,53] The Fermi level reference in UPS and IPES was established by a clean Au surface. Sub-nanosecond to nanosecond time-resolved studies were performed using a faster time correlated single photon counting (TCSPC) system (OB-900 L lifetime spectrometer, Edinburgh) with the excitation light source from the second harmonic generation (SHG, 400 nm) of pulse-selected femtosecond laser pulses at 800 nm (Tsunami and Model 3980 pulse picker, Spectra-Physics). Similar data analysis and fitting procedures are applied. The temporal resolution, after partial removal of the instrumental time broadening, is ~50 ps. Data were fitted with sum of exponential functions using the nonlinear least-squares procedure in combination with the convolution method. TM-AFM images were taken on a NanoScope IIIa controller (Veeco Metrology Group/Digital Instruments, Santa Barbara, CA), using a built-in software (version V6.13R1) to capture images. X-ray diffraction (XRD) pattern was collected using a Rigaku-TTRAX III diffractometer, operating at an accelerating voltage of 50 kV and current of 300 mA. A nickel (Ni)-filtered Cu Kα radiation source (0.154 nm) was used. A 4° min^{-1} scanning rate and a ~1.5–50° of scanning range at 2θ were carefully chosen to allow for complete X-ray penetration into the powdery PBDTQEH film.

Solar Cell Device Fabrication and Characterization.

Optimized solar cell devices used in this study were prepared by dissolving PBDTQEH and $PC_{71}BM$ (purchased from Nano-C) in 1,2-dichlorobenzene (DCB) in the weight ratios of 1:0.5, 1:1, and 1:2 with a PBDTQEH concentration of 14 mg mL^{-1}. For device fabrication, solution was stirred at 120 °C for more than 12 h to ensure complete dissolution. Patterned indium tin oxide (ITO)-coated glass substrates (Kintec Company, 15 Ω/square) were successively cleaned by ultrasonication in 1% neutral detergent in water, followed by deionized water, then acetone, and finally ethanol for 20 min each. The substrates were then dried and O_2 plasma cleaned immediately prior to the deposition of a 40-nm-thick layer of aqueous PEDOT:PSS PH500 (H.C. Starck) solution, as verified by a Filmetrics F10-RT-UV. Deposition of the PEDOT:PSS layer was followed by baking at 140 °C for 20 min. Substrates were subsequently transferred to an inert N_2-filled glove box (< 0.1 ppm O_2 and H_2O), and the active layer was spin-coated. The wet film was slowly dried in a covered Petri dish for a certain time and subsequently annealed at 140 °C for 10 min in the glove box. The coated substrates were then transferred to a thermal evaporator and evacuated to $\leq 5 \times 10^{-6}$ Torr before a 30-nm-thick calcium layer followed by a 100-nm aluminum electrode layer were deposited. The active area of each device was 0.04 cm^2 with a length:width ratio of 1:1. The conventional device was encapsulated in a nitrogen-filled

glove box with UV epoxy and cover glass. Inverted PSCs were fabricated in a configuration of glass/ITO/ZnO/PBDTQEH:$PC_{71}BM$/MoO_x/Ag. The ITO-coated glass substrates were first cleaned with the same procedures as conventional structure devices. The ZnO precursor was prepared using zinc acetate dehydrate ($Zn(CH_3COO)_2{\cdot}2H_2O$, Aldrich, 99.999%) as starting material, and isopropyl alcohol and monoethanolamine (MEA, Aldrich, 99.7%) as the non-toxic solvent and stabilizer under vigorous stirring for 12 h for the hydrolysis reaction in air. The respective solutions were spin-coated on glass substrates at 5000 rpm for 40 s and preheated at 280 °C for 10 min in air to remove residual organic materials. The PBDTQEH:$PC_{71}BM$ films with optimal concentration and preparing conditions in conventional structure devices were then spin-coated on top of ZnO layers in the nitrogen-filled glove box. The thickness of active layer in organic solar cell is about 150 nm measured by a profilometer (Ambios Tech.XP-2). After slow drying of active films for a certain time, the samples were annealed at 140 °C for 10 min before MoO_x and anode metal depositions. Then, thin layer of MoO_x films (1.5 nm) were thermally evaporated (0.03 nm s^{-1}) using a crucible on top of the active layers. Finally, the Ag anodes (85 nm) were deposited (0.1 nm s^{-1}) from a tungsten boat under a pressure of 5×10^{-6} Torr. The *J*–*V* curves were measured with a Newport–Oriel (Sol3A Class AAA Solar Simulators) AM 1.5G light source operating at 100 mW cm^{-2}, and independently cross-checked using a 300-W AM 1.5G source operating at 100 mW cm^{-2} for verification. The light intensity was determined by a monosilicon detector (with KG-5 visible color filter) calibrated by the National Renewable Energy Laboratory (NREL) to minimize spectral mismatch. Hole mobility was measured according to a method based on the space charge limited current (SCLC) model described in the literature,[54,55] using a diode configuration of ITO/PEDOT:PSS/polymer:$PC_{71}BM$/Pd. The SCLC current was measured under dark conditions using a Keithley Model 2400 unit. The IPCE spectra were measured using a lock-in amplifier with a current preamplifier under short-circuit conditions. The devices were illuminated by monochromatic light from a xenon lamp passing through a monochromator with a typical intensity of 30 μW. A calibrated monosilicon diode with known spectral response was used as a reference.

Results and discussion

The synthesis routes of the target polymer are depicted in Scheme 1. PBDTQEH was synthesized in good yield by a Stille coupling reaction using $Pd(PPh_3)_4$ as a catalyst under the microwave heating condition shown in the Supporting Information. The crude polymer was precipitated into methanol and filtered, followed by careful extraction with methanol, acetone, dichloromethane and chloroform with Soxhlet apparatus to remove byproducts and oligomers. The final product was obtained via extraction from the chloroform fraction precipitated into methanol, filtered and dried under vacuum for 12 h. This method gave the desired polymer in greater than 80% yield. PBDTQEH manifests an excellent film-casting property as well as good solubility in common halogenated solvents. The molecular weight M_n of the synthesized copolymer PBDTQEH was determined by gel permeation chromatography (GPC) using a polystyrene standard in tetrahydofuran (THF) eluent, and was found to be 57.8 kg mol^{-1} with a polydispersity index (PDI) of 2.03. Thermal stability of the PBDTQEH was confirmed by thermogravimetric analysis (TGA) at a temperature ramp rate of 10 °C min^{-1} under N_2. (Fig. S4 in the ESI†). The onset decomposition temperature of PBDTQEH at 5% weight loss is 317 °C, indicating a high thermal stability appropriate for long-term photovoltaic and optoelectronic applications.

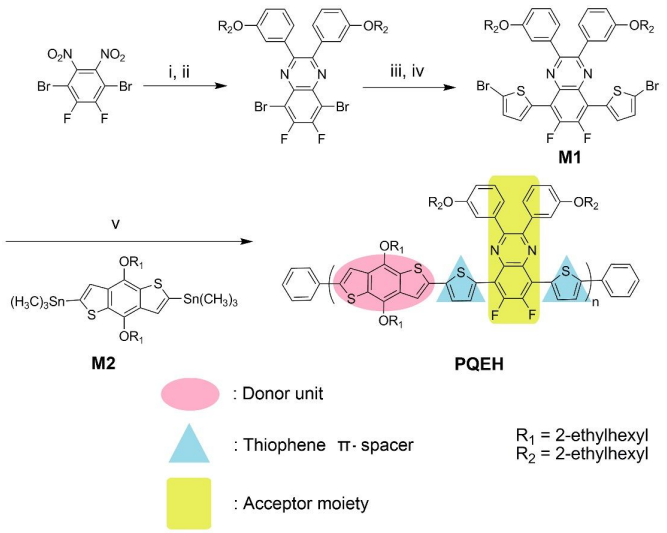

Scheme 1. Synthetic route adopted for the preparation of monomers and polymers. Reagents and conditions: (i) Fe, AcOH 50 ºC, 4 h; (ii) 1,2-bis(3-((2-ethylhexyl)oxy)phenyl)ethane-1,2-dione, AcOH, reflux overnight; (iii) 2-(tributylstannyl) thiophene, $PdCl_2(PPh_3)_2$, toluene, reflux, 24 h; (iv) NBS, DMF, 40 ºC, 5h; (v) $Pd(PPh_3)_4$, toluene, reflux, 36 h.

The optical properties of the PBDTQEH polymer were investigated by UV-vis absorption spectroscopy in solution and as thin film. Relevant data are summarized in Table 1. As shown in Fig. 1a, PBDTQEH in dilute 1,2-dichlorobenzene (DCB) solution exhibits a broad and strong absorption spectral feature across the entire UV-vis region with three major absorption peaks located at 412, 564 and 593 nm. The shorter wavelength peak is assigned to the localized π-π* transitions, whereas the lower energy band corresponds to the intramolecular charge transfer (ICT) between D and A moieties of the polymer backbone. To provide an in-depth insight into the molecular orbital distributions of the polymer, a density functional theory (DFT) calculation at the B3LYP/6-31G* level, was performed on dimers with methyl substituted alkyl chains for simplicity. The optimized geometry and the resulting frontier molecular orbitals of PBDTQEH are depicted in Fig.1c. As seen in the top-view and side-view graphs of Fig. 1c, the backbone of PBDTQEH exhibits nearly coplanar conformation, which is beneficial to intrinsic π-π stacking and charge transfer. Moreover, the energy-minimized dihedral angels of BDT-thiophene and QEH-thiophene in each repeating unit of PBDTQEH are 2.7° and 8.6°, respectively. The electron density in the HOMO wave function is distributed along the whole conjugated backbone of the polymer, whereas the LUMO electron density is mostly localized upon the QEH moiety. This analysis provides sufficient evidence of the formation of a D-π-A structure and the ICT behavior of the material. In the solid state, however, the backbone twist is restricted due to planarizing intramolecular interactions between the nitrogen atom on the quinoxaline moiety and the π-spacer sulfur atom on the neighboring unit, as manifested by the appearance of absorption vibronic structure, which is red-shifted by 21 nm in comparison to the solution absorption spectrum (see Fig. 1a). Both increased intermolecular π-π stacking of polymer chains and planarity in the polymer backbone could be beneficial for improving the charge carrier mobility of the resulting films. Furthermore, the absorption edge (λ_{edge}) of PBDTQEH film is 685 nm, from which the optical bandgap (E_g^{opt}) of PBDTQEH, deduced from the onset of absorption in the solid state, is calculated to be 1.81 eV (Table 1). Fig. 1b

exhibits the X-ray diffraction pattern of the PBDTQEH pristine film. The Bragg scattering peak of (100) appears relatively strong in intensity at $2\theta = 4.10°$ with a d_{100} spacing of 21.53 Å, corresponding to a periodic and self-organized lamellar structure, with an interlayer spacing between two PBDTQEH backbones separated by the branched alkyl side chains. Additionally, PBDTQEH polymer revealed a distinctive (010) reflection at $2\theta = 23.84°$ with a d_{010} spacing of 3.73 Å, corresponding to the cofacial interlayer π-π stacking packing between the conjugated main chains. The amorphous hump typically observed near 20~30° appears to be very weak. This result suggests that the PBDTQEH polymer is highly crystalline in spite of the fact that the presence of closer interdigitation of the branched ethylhexyl side-chains attached to the polymer backbones.

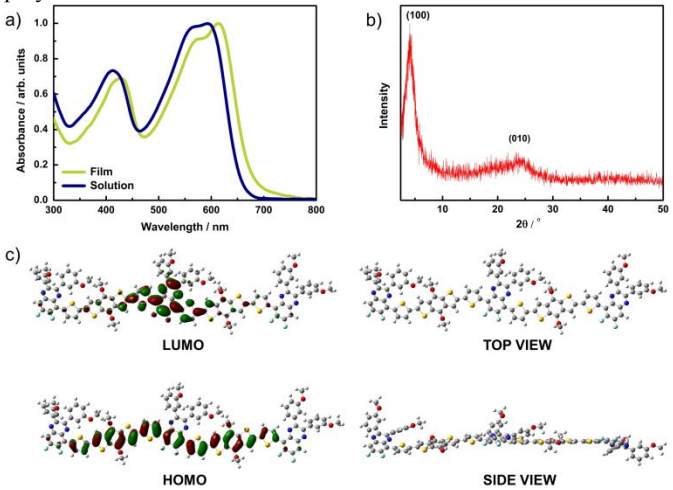

Fig. 1. a) UV-vis absorption spectra of PBDTQEH copolymer in 1,2-dichlorobenzene solution and as a film. b) X-ray diffraction pattern of powdery PBDTQEH film. c) Molecular conformation of designed PBDTQEH copolymer was anticipated from the dimers conformation calculation under minimized energy state, and the methyl-substituted dimers' frontier molecular orbital surfaces are also illustrated.

Table 1. Optical and electrochemical properties of PBDTQEH.

Polymer	λ_{max} [nm]	λ_{max} [nm]	λ_{edge} [nm]	E_g^{opt} [eV][a)]	E_{HOMO} [eV][b)]	E_{LUMO} [eV][c)]
	Solution	Film	Film			
PBDTQEH	412, 564, 593	427, 570, 614	685	1.81	-5.35	-3.40

[a)]Estimated from the onset of UV-vis spectrum of the film; [b)]Determined from the onset of UPS spectrum of the film; [c)]Calculated from the onset of IPES spectrum of the film.

The combined ultraviolet photoemission spectroscopy (UPS) and inverse photoemission spectroscopy (IPES) of PBDTQEH film are shown in Fig. 2a, whereas the Fermi level (E_F) was used as the reference energy. The photoemission onset of secondary electrons is displayed in the left, and the vacuum level can be obtained by adding the energy of excitation photons (21.2 eV) to the energy of the onset. The ionization energy (IE) and electron affinity (EA) of PBDTQEH can then be directly obtained from the positions of the onsets of filled and empty states. The HOMO edge is 0.85 eV below E_F, corresponding to an IE valve of -5.35 eV, while the LUMO edge is 1.1 eV above E_F, leading to an EA of -3.40 eV. It is noteworthy that the PBDTQEH polymer not only exhibits a deeply low-lying HOMO energy level against oxidization but also is in an ideal range to obtain a higher V_{oc}. Because the V_{oc} value for PSCs can be expressed by the empirical equation: $V_{oc} = e^{-1} \times (|E_{HOMO}^{donor}| - |E_{LUMO}^{acceptor}| - 0.3\ eV)$, where e is the elementary charge, E is the energy level and 0.3 eV is an empirical value for efficient charge separation.[42,43] Absolutely, the introduction of electron-deficient fluorine atoms can further lower both the HOMO and LUMO energy levels, and the result agrees well with the previous reports.[3,11,31] A similar polymer reported by Duan et al. but without fluorine substitution shows a relatively high-lying of HOMO value (5.12 eV), LUMO value (3.38 eV), and a red shift of UV-vis absorption spectrum as compared with PBDTQEH,[44] providing the direct evidence that the introduction of F atoms to the quinoxaline moiety is effective to further lower the energy levels of resulting polymer. The relatively low-lying HOMO level and medium bandgap, along with good solubility, advantageous geometry, and good charge carrier transport, could act as an effective donor component for BHJ solar cells (*vide infra*). Furthermore, the LUMO energy level is positioned well above the LUMO energy level of $PC_{71}BM$ (-4.0 eV) with a desired energy offset ΔE_{LUMO} ($E_{LUMO}^{acceptor} - E_{LUMO}^{donor}$) > 0.3eV, ensuring efficient exciton dissociation and charge separation without too much energy loss.[43]

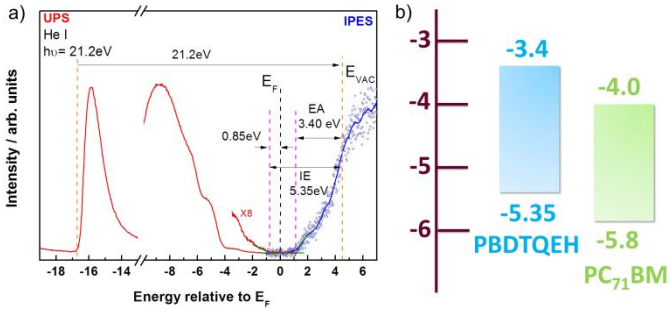

Fig. 2. a) Ultraviolet photoemission spectroscopy (UPS) and inverse photoemission spectroscopy (IPES) of PBDTQEH film. b) Energy level diagram of PBDTQEH and $PC_{71}BM$. The highest occupied molecular orbital (HOMO) and the lowest unoccupied molecular orbital (LUMO) energy levels of PBDTQEH are taken from UPS and IPES, respectively.

The quenching of polymer photoluminescence (PL) upon the addition of a fullerene acceptor is often considered to reflect the ability of polymer excitons reaching the polymer:fullerene interfaces within their lifetime. The solid-state PL spectrum of PBDTQEH exhibits a strong emission peak at 756 nm (see Fig. 3a). After adding $PC_{71}BM$ with various blend ratios, over 99% of the PBDTQEH PL is completely quenched, even with a small weight percent of fullerene, which was accompanied with a much shorter PL decay time (*vide infra*). This indicates not only the absence of very large polymer domains but also a profound ultrafast photoinduced electron transfer from the polymer to the fullerene in the PBDTQEH:$PC_{71}BM$ blends (Fig. 2b). Fig. 3b illustrates the decay traces of the PBDTQEH pristine film and 1:1 blends processed with and without DIO additives. Again, the strong PL quenching can be explained by rapid energy transfer from PBDTQEH to fullerene. For the blends without DIO additives, in addition to the drastic diminishing of the PBDTQEH PL spectrum, a broad and much red-shifted PL band appears with a maximum at ~880 nm, suggesting a direct radiative decay of the interfacial charge transfer states.[22-29] Based on the 3% DIO additive and under the same experimental condition, we could barely resolve the 880 nm interfacial charge transfer emission, implying much faster interfacial charge separation facilitated by DIO addition.

To gain further insight into the differences in the forward charge transfer of the blends, time-resolved PL experiments were performed with a time correlated single photon counting (TCSPC) technique and the results are shown in Fig. 4. The emission (monitored at 750 nm) for the pristine PBDTQEH film showed a single exponential decay dynamics, which was then fitted to be 505 ps. Upon monitoring at 750 nm emission, the PL decay of the 1:1 PBDTQEH:$PC_{71}BM$ blend without DIO additive reveals bi-exponential kinetics with a fast decay component that is beyond the time of instrument response function (IRF < 50 ps), accompanied by a tailing component of 410 ps. In comparison, the emission of the 1:1 blend with 3% DIO additive showed a system-response-limit decay component (< 50 ps) and a very small percentage of tailing component which was fitted to be ~310 ps. For both blends, on the one hand, it is reasonable to ascribe the system unresolvable decay component to the fast rate of initial photoinduced charge transfer. It is noteworthy that photoinduced charge transfer is well known to occur on sub-picosecond time scales in devices with a large driving free energy for charge transfer.[45] On the other hand, we tentatively assign the long-lived component to the signature of charge transfer state emission.[22-29] The faster and small ratio of charge transfer emission in the DIO added blend indicates more efficient exciton dissociation. The addition of a small amount of DIO results in an enhancement in separation of photogenerated electron-hole pairs, arising from the fact that the sufficiently fine morphology of the blends could ensure phogenerated excitons reaching to the D/A interfaces followed by efficient excitons separation.

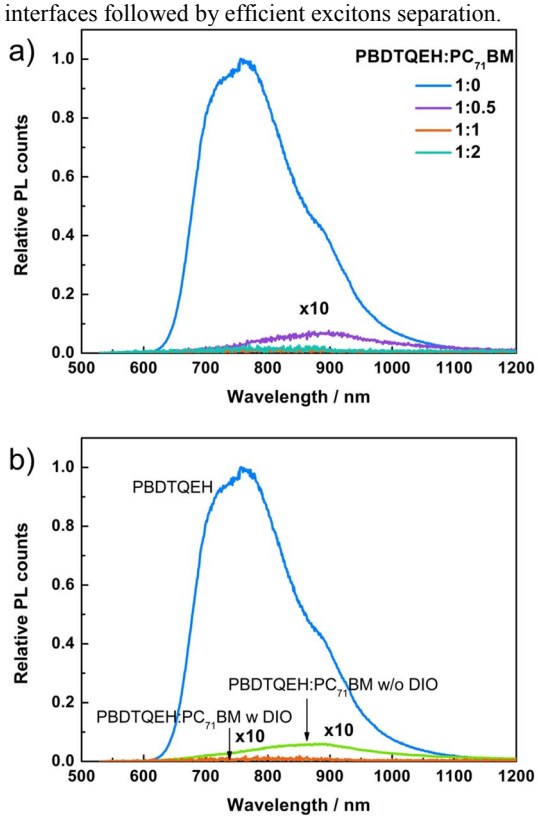

Fig. 3. a) Normalized photoluminescence spectra of the pristine PBDTQEH film and blends with various blend ratios prepared with 3% DIO. b) Normalized photoluminescence spectra of the neat PBDTQEH film and 1:1 PBDTQEH:$PC_{71}BM$ blend films with and without DIO addition.

With the desired good solubility and high efficient solar light absorption, photovoltaic properties of polymer were initially investigated based on PSCs with the conventional device architecture consisting of ITO/PEDOT:PSS/PBDTQEH:$PC_{71}BM$ (1:0.5, 1:1 and 1:2, *w*/*w*)/Ca/Al were fabricated and tested under the illumination of AM 1.5G at 100 mW cm^{-2}. The asymmetric $PC_{71}BM$ was chosen instead of $PC_{61}BM$ due to its stronger light absorption in the visible region. The best current density–voltage (*J*–*V*) curves of the resulting devices with various blend ratios are depicted in Fig. 5a and the corresponding photovoltaic performances are summarized in Table 2. The optimized blend of PBDTQEH:$PC_{71}BM$ in a 1:1 weight ratio gave a decent PCE of 4.23%, with a V_{oc} of 0.82 V, a J_{sc} of 10.03 mA cm^{-2}, and a FF of 51.4%. The above photophysical studies have shown the increase of chrage transfer efficiency upon addition of DIO to the active layer due to its ability to solvate the fullerenes. Together with the high boiling point (363 °C under atmospheric pressure), optimizing DIO may lead to a comprehensive impact on J_{sc} by providing more optimal morphology for facilitating charge carrier transportation.[46,47] With addition of 3% DIO, the 1:1 blend of PBDTQEH:$PC_{71}BM$ yielded a best PCE of 5.90%, with a V_{oc} of 0.78 V, a J_{sc} of 13.42 mA cm^{-2}, and a FF of 56.4%. Overall, our devices data along with the PL spectra shown in Fig.3b (*vide supra*), suggest that devices with 3% DIO additive exhibited better PCEs than that of the devices without any additive. This is mainly due to the reduction in charge carrier recombination and enhancement in forward charge transfer (*vide supra*), resulting in enhancements in both J_{sc} and FF. It is also worth noting that addition of processing additive reduced the V_{oc} of devices to some extent due to the upward shift in the HOMO energy level of polymer as a result of polymer aggregation.[48,49] The comparative difference in device performance in terms of the J_{sc} and FF with and without DIO additives is most likely due to the optimization of blend morphology together with the discrepancy in charge carrier mobility elaborated as follows.

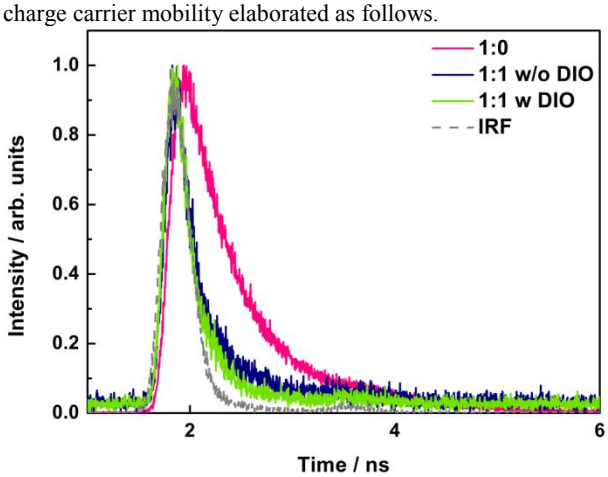

Fig. 4. Time-resolved photoluminescence decays monitored at 730 nm for neat PBDTQEH film and PBDTQEH:$PC_{71}BM$ blend films with and without DIO additive, along with the instrument response function (IRF) and the excitation wavelength is 400 nm.

From the tapping-mode atomic force microscopy (TM-AFM) images shown in Fig. S5 of the ESI†, we observed that the blends without additive present highly dense polymer phase zone throughout the surface but lack uniform phase separation between the polymer and $PC_{71}BM$. The latter may hinder vertical exciton separation and charge transport, block the electron collected by cathode, and consequently deteriorate the device performances including the J_{sc} and FF. In sharp contrast, the addition of DIO demonstrated a similar surface morphology but possessed both uniform and fine features of phase separation between the two materials with root-mean-square (RMS) roughness values of 1.92-3.23 nm (Fig. 6). Additionally, the distinct spacing of the bicontinuous fibrillar interpenetrating morphologies, possibly owing

to the strong π-π intermolecular interactions (*vide supra*), has a lateral dimension ranging from 18 to 22 nm, which is close to the ideal magnitude of the exciton diffusion length, and could effectively benefit charge transport prior to recombination.[50]

Table 2. Representative photovoltaic performance of conventional and inverted structure devices with various PBDTQEH:$PC_{71}BM$ blend ratios under AM 1.5G solar illumination.

Conventional Structure	Device	D/A ratio	Solvent	V_{oc} [V]	J_{sc} [mA cm^{-2}]	FF [%]	PCE_{max} (PCE_{ave})[c] [%]
	D1	1:0.5	DCB	0.84	9.49	43.1	3.44 (3.35)
	D2	1:0.5	DCB + 3% DIO	0.81	10.20	46.7	3.86 (3.72)
	D3	1:1	DCB	0.82	10.03	51.4	4.23 (4.10)
	D4	1:1	DCB + 3% DIO	0.78	13.42	56.4	5.90 (5.82)
	D5	1:2	DCB	0.85	9.81	45.4	3.79 (3.69)
	D6	1:2	DCB + 3% DIO	0.77	10.81	51.7	4.31 (4.23)
Inverted Structure	Device	D/A ratio	Solvent	V_{oc} [V]	J_{sc} [mA cm^{-2}]	FF [%]	PCE_{max} (PCE_{ave}) [%]
	D7[a]	1:1	DCB + 3% DIO	0.79	11.67	59.0	5.42 (5.31)
	D8[b]	1:1	DCB + 3% DIO	0.78	12.72	64.3	6.36 (6.22)

[a] Device performance of inverted structure PSC with two electron-transporting layers; [b] Device performance of inverted structure PSC with five electron-transporting layers; [c] Only the optimized recipes were considered for the estimation of the average PCE; data have been averaged over 10 devices.

Insights into the discrepancy in charge carrier mobilities of polymer blends were measured in vertical hole-only devices using the space-charge-limited current (SCLC) model at low voltage. The measured hole mobility for 1:0.5, 1:1 and 1:2 blends is 6.4×10^{-4} , 1.2×10^{-3} and 8.8×10^{-4} cm^2 V^{-1} s^{-1} , respectively (Fig. S6, ESI†). The relative higher hole mobility of 1:1 blend yields a balanced charge carrier transport in the active layer and is expected to contribute, in part, to the high J_s in optimized BHJ devices. When considering that high charge mobility is favorable for the reduction of recombination of excitons, it is expected that device based on the 1:1 blend will result in higher FF and J_{sc}. Therefore, the intimately mixed and well-ordered domains within the matrix, together with the high hole carrier mobility of the material, are likely to enable efficient charge separation and transport, and could help to explain the good performance of the PSCs.

To verify the accuracy of the photo *J–V* measurements, the corresponding incident photon-to-current efficiency (IPCE) spectra of the devices elaborated above were measured under illumination of monochromatic light shown in Fig. 5b. According to the PSC devices fabricated with various PBDTQEH:$PC_{71}BM$ blend ratios, very broad panchromatic spectra over the entire excitation spectral range were obtained from IPCE measurements. The trend in IPCE roughly tracks that observed in J_{sc}, in which 1:0.5 blend presents the lowest quantum efficiency and 1:1 blend exhibits the highest. The optimum device of 1:1 blend has a maximum value at 70.6% at around 558 nm and a broad photoresponse of over 60% in the 368-634 nm range, as well as indicates that the active layer is photosensitive beyond 730 nm, thereby enabling it to harvest light across the entire visible spectrum. Moreover, the IPCE spectra accord well with the UV-vis absorption spectra of the blends (Fig. S7 in the ESI†), showing a close correlation with the photocurrents. The integral J_{sc} of devices with blend ratios of 1:0.5, 1:1 and 1:2 from IPCE spectra are 9.58, 12.24 and 9.98 mA cm^{-2}, respectively. The J_{sc} values calculated from integration of the IPCE spectra are within 5-10%, which closely match the J_{sc} values obtained from the *J–V* measurements under white light illumination, supporting the reliability of the photovoltaic measurement.

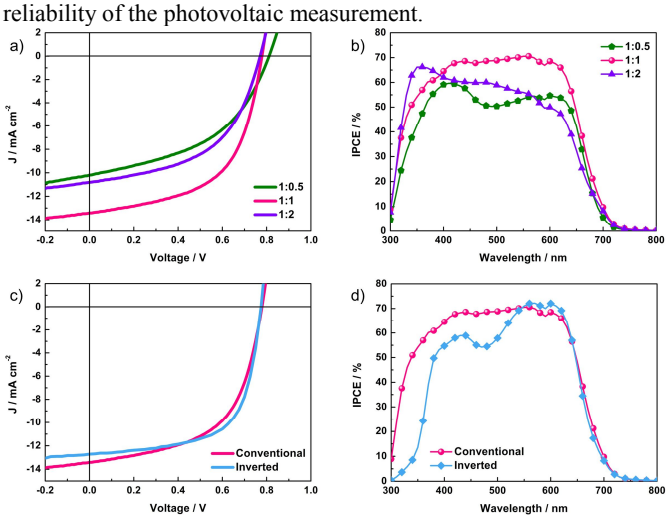

Fig. 5. a) Current density–voltage (*J–V*) characteristics of optimized conventional devices made from different blend ratios of PBDTQEH:$PC_{71}BM$ measured under AM 1.5G illumination at 100 mW cm^{-2}. For the 1:0.5 device: V_{oc} = 0.81 V, J_{sc} = -10.20 mA cm^{-2}, FF = 46.7%, and PCE = 3.86%. For the 1:1 device: V_{oc} = 0.78 V, J_{sc} = -13.42 mA cm^{-2}, FF = 56.4%, and PCE = 5.90%. For the 1:2 device: V_{oc} = 0.77 V, J_{sc} = -10.81 mA cm^{-2}, FF = 51.7%, and PCE = 4.31%. b) IPCE spectra of optimized conventional devices made from different blend ratios of PBDTQEH:$PC_{71}BM$ illuminated by monochromatic light. c) *J–V* curves of 1:1 PBDTQEH:$PC_{71}BM$ solar cells with conventional device (pink) and inverted device (sky-blue) under AM 1.5G solar illumination. d) Corresponding IPCE spectra of optimized 1:1 PBDTQEH:$PC_{71}BM$ solar cells made

from conventional and inverted devices illuminated by monochromatic light.

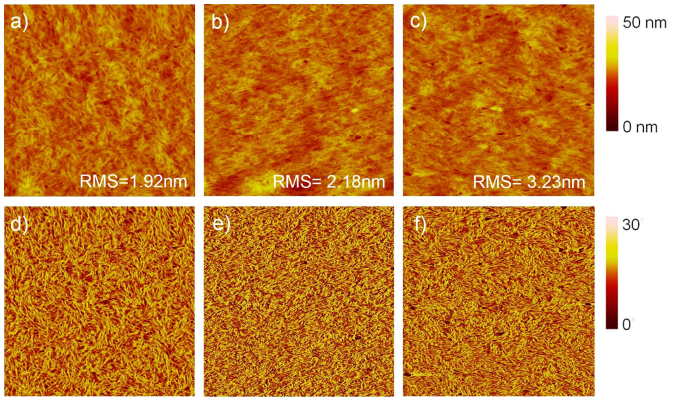

Fig. 6. Morphology characterization of conventional devices. TM-AFM (a–c) topography and (d–f) phase images of PBDTQEH:$PC_{71}BM$ blend films with 3% DIO in various compositions: (a, d) 1:0.5, (b, e) 1:1, and (c, f) 1:2. The imaging size is 2 μm × 2 μm.

Compared to conventional PSCs, further performance optimization was studied on the inverted device geometry of ITO/ZnO/polymer:$PC_{71}BM$ (1:1, *w*/*w*)/MoO_3/Ag, which possesses better long-term ambient stability because the acidic PEDOT:PSS layer is replaced by other stable anode buffer layers (e.g. ZnO) and the more stable high work-function metal electrode (e.g. Ag) is used (*vide infra*). When the five layers of ZnO thin film of device D8 were added as the electron extraction layers in comparison with two buffer layers of ZnO thin film of D7, the resulting D8 device exhibited an enhanced J_{sc} of 12.72 mA cm^{-2} along with an obviously improved FF of 64.3%, yielding a further improved PCE of up to 6.36% (Table 2). To understand the sharp difference in the solar cell performance, TM-AFM images shown in Fig. 7 were conducted to investigate their morphologies of the devices thoroughly. It can be clearly observed that the surface of active layer spin-coated onto the 2-layer ZnO film (Fig. 7a and c) demonstrates rather rough surface with a RMS value of 4.02 nm and also presents inferior morphology with larger aggregations. This dissatisfactory morphology decreased the phase-separated interfacial areas for efficient exciton dissociation, and thus diminished the device performance. In contrast, the surface of active layer spin-coated onto the 5-layer ZnO film (Fig. 7b and d) leads to relatively smooth surface in conjunction with a RMS value of 2.91 nm, and reveals finer percolation pathways that can facilitate charge transport to the respective electrodes and thereby leads to increased J_{sc}. Therefore, we speculate that the distinctly increased J_{sc} and FF may origin from the fact that a more uniform surface reduced the bimolecular recombination and suppressed the formation of shunt paths directing from a cathode to an anode. Also, the increasing conductivity of stacking buffer layers formed a better path for exciton extraction and diminished the series resistance of the overall device. The highest PCE achieved from the inverted PSC was 6.36% (Fig. 5c), which is substantially higher than the value achieved from the conventional device. The enhancement is principally due to the substantial difference in the FF value. In addition, the IPCE characteristic of inverted device reveals a vast photoresponse with a maximum value of 72.17% at the wavelength of 570 nm and illustrates higher photoconversion efficiencies over 50% throughout the range from 380 to 647 nm (Fig. 5d). The calculated J_{sc} values by integrating the IPCE data were 12.24 and 11.20 mA cm^{-2} for the conventional and inverted devices, respectively. It is noteworthy that the significant drop in the IPCE spectrum of inverted device in the range between 300 and 550 nm, which causes the sacrifice of J_{sc} as compared with the conventional device, can be attributed to the loss of transmittance resulting from the absorption of ZnO film.[51]

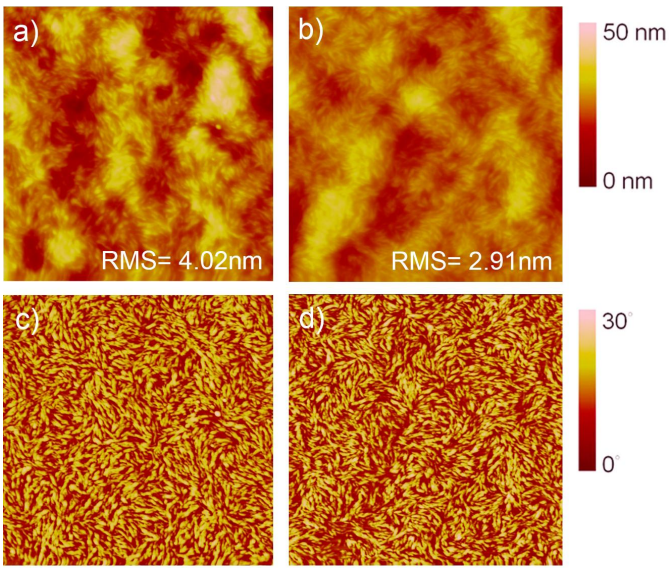

Fig. 7. TM-AFM topography (upper row) and phase (lower row) images of a,c) two ZnO layers and b,d) five ZnO layers on the bottom of 1:1 PBDTQEH:$PC_{71}BM$ blends.

To further explore the potential of PBDTQEH-based PSCs for commercialization, the device performances in both conventional and inverted configurations were recorded as a function of exposure time in air and the corresponding results are shown in Fig. 8a. To reveal the long-term stability of the polymer, devices with inverted structure were stored in atmosphere without any encapsulation. The lifetime of conventional device demonstrates a rapid degradation as compared with that of the inverted device in consequence of the highly oxidative metal cathode[35,36] and both of the hygroscopic and strong acidic nature of the PEDOT:PSS.[37,38] Furthermore, it was observed that the solar efficiency of the conventional device quickly dropped to ~ 0% after air exposure for merely 240 h. Conversely, the solar performance of the inverted device still exhibited a high PCE of 4.72% (degradation to 74.2% of initial PCE) even after being stored without encapsulation in air at *ca*. 50% relative humidity for over 1000 h (Fig. 8a). This suggests that the inverted cell architecture functions an efficient passivation property against the oxygen and moisture, and also confirms the stable nature of PBDTQEH copolymer due to the deep HOMO energy level. This result also indicates that the stability of PBDTQEH-based PSCs is actually better than the polymer PBDT-TFQ we reported before (see Fig. S8 in ESI†). The *J*–*V* characteristic of the inverted cell as a function of storage time in ambient air is depicted in Fig. S9 of the ESI† and the key parameters are summarized in Table S1 (see ESI†). The degradation of inverted solar cell is dominated by the J_{sc} and FF shown in Fig. 8b. Nevertheless, the inverted device reveals a J_{sc} decay of only 25% in ambient air after 1500 h. Besides, it was found that the V_{oc} decreased after 1000 h but remained at 0.76 V even after storage in ambient air for over two months (1500 h). From this point of view, our results clearly demonstrate a promising way for the fabrication of PBDTQEH:$PC_{71}BM$ BHJ solar cells with high efficiency and excellent long-term stability.

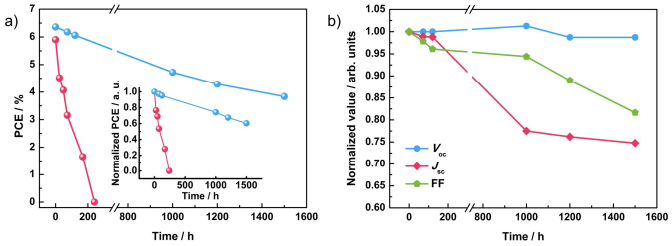

Fig. 8. a) Air stability tests of PBDTQEH:$PC_{71}BM$ solar cells upon conventional (red line) and inverted (blue line) configurations in ambient atmosphere as a function of storage time. The inverted PBDTQEH:$PC_{71}BM$ devices stored in air without any encapsulation. These devices were stored in a cabinet with a relative humidity at *ca*. 50%. The inset shows the normalized efficiency decay. b) Inverted solar cell characteristic, normalized by their initial values as a function of storage time in ambient air.

Conclusion

In conclusion, a new, yet efficient, π-conjugated D-A copolymer PBDTQEH, which incorporates a fluorinated quinoxaline moiety with branched side chains, forming a more robust morphology, has been synthesized and thoroughly characterized. PBDTQEH copolymer not only offers excellent solubility and thermal stability, but it also exhibits many desirable advantages of deep HOMO and LUMO energy levels, long-term air-stability, semicrystallinity, and high hole mobility. A detailed study regarding the structure-function relationship in the PSCs was also explored. High photovoltaic performance with 5.90% and 6.36% could be obtained for 1:1 PBDTQEH:$PC_{71}BM$ blends in conventional and inverted device architectures, respectively. More importantly, inverted device degrades to 74% of initial PCE value after storage in ambient air for over 1000 h without any encapsulation, which reveals a promising candidate for future development of high-efficiency and practical polymer solar cells.

Acknowledgements

This work was supported by the Ministry of Science and Technology of Taiwan. The authors thank Prof. Shih-Huang Tung and Chung-Hao Liu, National Taiwan University, for the TM-AFM support.

Notes and references

[a] *Department of Chemistry, National Taiwan University, Taipei, 106, Taiwan. E-mail: austinchen@ncu.edu.tw; chop@ntu.edu.tw; Tel: +886 2 3366 3894*
[b] *Department of Electrical Engineering and Graduate Institute of Electrooptical Engineering, National Taiwan University, Taipei, 106, Taiwan. E-mail: chihiwu@cc.ee.ntu.edu.tw; Tel: +886 2 3366 3656*
[c] *Center of Emerging Material and Advanced Devices, National Taiwan University, Taipei, 106, Taiwan.*

† Electronic Supplementary Information (ESI) available: Synthesis details, device fabrication procedures, thermogravimetric analysis, TM-AFM images, hole mobility, UV−vis spectra, and current–voltage measurements. See DOI: 10.1039/b000000x/

1 S. R. Forrest, *Nature*, 2004, **428,** 911-918.
2 B. C. Thompson and J. M. J. Fréchet, *Angew. Chem. Int. Ed.*, 2008, **47,** 58-77.
3 H. J. Son, W. Wang, T. Xu, Y. Liang, Y. Wu, G. Li and L. Yu, *J. Am. Chem. Soc.*, 2011, **133,** 1885-1894.
4 L. Huo, X. Guo, S. Zhang, Y. Li and J. Hou, *Macromolecules*, 2011, **44,** 4035-4037.
5 H.-C. Chen, I-C. Wu, J.-H. Hung, F.-J. Chen, I-W. P. Chen, Y.-K. Peng, C.-S. Lin, C.-h. Chen, Y.-J. Sheng, H.-K. Tsao and P.-T. Chou, *Small*, 2011, **7,** 1098-1107.
6 J. Liu, L. Chen, B. Gao, X. Cao, Y. Han, Z. Xie and L. Wang, *J. Mater. Chem. A*, 2013, **1,** 6216-6225.
7 H.-C. Chen, S.-W. Chou, W.-H. Tseng, I-W. P. Chen, C.-C. Liu, C. Liu, C.-L. Liu, C.-h. Chen, C.-I Wu and P.-T. Chou, *Adv. Funct. Mater.*, 2012, **22,** 3975-3984.
8 M. Wang, X. Hu, P. Liu, W. Li, X. Gong, F. Huang and Y. Cao, *J. Am. Chem. Soc.*, 2011, **133,** 9638-9641.
9 S.-H. Kao, Z.-L. Tseng, P.-Y. Ho, C.-Y. Kao, S. Thiyagua and C.-F. Lin, *J. Mater. Chem. A*, 2013, **1,** 14641-14648.
10 T.-Y. Chu, J. Lu, S. Beaupré, Y. Zhang, J.-R. Pouliot, J. Zhou, A. Najari, M. Leclerc and Y. Tao, *Adv. Funct. Mater.*, 2012, **22,** 2345-2351.
11 H. Zhou, L. Yang, A. C. Stuart, S. C. Price, S. Liu and W. You, *Angew. Chem. Int. Ed.*, 2011, **50,** 2995-2998.
12 H.-C. Chen, Y.-H. Chen, C.-H. Liu, Y.-H. Hsu, Y.-C. Chien, W.-T. Chuang, C.-Y. Cheng, C.-L. Liu, S.-W. Chou, S.-H. Tung and P.-T. Chou, *Polym. Chem.*, 2013, **4,** 3411-3418.
13 Y. He, H.-Y. Chen, J. Hou and Y. Li, *J. Am. Chem. Soc.*, 2010, **132,** 1377-1382.
14 M. Lenes, G.-J. A. H. Wetzelaer, F. B. Kooistra, S. C. Veenstra, J. C. Hummelen and P. W. M. Blom, *Adv. Mater.*, 2008, **20,** 2116-2119.
15 S. A. Backer, K. Sivula, D. F. Kavulak and J. M. J. Fréchet, *Chem. Mater.*, 2007, **19,** 2927-2929.
16 H.-C. Chen, C.-W. Lai, I-C. Wu, H.-R. Pan, I-W. P. Chen, Y.-K. Peng, C.-L. Liu, C.-h. Chen and P.-T. Chou, *Adv. Mater.*, 2011, **23,** 5451-5455.
17 H. Wei, H. Zhang, G. Jin, T. Na, G. Zhang, X. Zhang, Y. Wang, H. Sun, W. Tian and B. Yang, *Adv. Funct. Mater.*, 2013, **23,** 4035-4042.
18 F. Gao, S. Ren and J. Wang, *Energy Environ. Sci.*, 2013, **6,** 2020-2040.
19 Z. Chen, H. Zhang, W. Yu, Z. Li, J. Hou, H. Wei and B. Yang, *Adv. Energy Mater.*, 2013, **3,** 433-437.
20 Z. Liu, Y. Sun, J. Yuan, H. Wei, X. Huang, L. Han, W. Wang, H. Wang and W. Ma, *Adv. Mater.*, 2013, **25,** 5772-5778.
21 C. Kitamura, S. Tanaka and Y. Yamashita, *Chem. Mater.*, 1996, **8,** 570-578.
22 M. A. Loi, S. Toffanin, M. Muccini, M. Forster, U. Scherf and M. Scharber, *Adv. Funct. Mater.*, 2007, **17,** 2111-2116.
23 I.-W. Hwang, D. Moses and A. J. Heeger, *J. Phys. Chem. C*, 2008, **112,** 4350-4354.
24 D. Veldman, O. Ipek, S. C. J. Meskers, J. Sweelssen, M. M. Koetse, S. C. Veenstra, J. M. Kroon, S. S. van Bavel, J. Loos and R. A. J. Janssen, *J. Am. Chem. Soc.*, 2008, **130,** 7721-7735.
25 M. Hallermann, I. Kriegel, E. Da Como, J. M. Berger, E. von Hauff and J. Feldmann, *Adv. Funct. Mater.*, 2009, **19,** 3662-3668.
26 D. Veldman, S. C. J. Meskers and R. A. J. Janssen, *Adv. Funct. Mater.*, 2009, **19,** 1939-1948.
27 T. M. Clarke and J. R. Durrant, *Chem. Rev.*, 2010, **110,** 6736-6767.
28 M. C. Scharber, C. Lungenschmied, H.-J. Egelhaaf, G. Matt, M. Bednorz, T. Fromherz, J. Gao, D. Jarzab and M. A. Loi, *Energy Environ. Sci.*, 2011, **4,** 5077-5083.
29 D. Jarzab, F. Cordella, J. Gao, M. Scharber, H.-J. Egelhaaf and M. A. Loi, *Adv. Energy Mater.*, 2011, **1,** 604-609.

30 Z. He, C. Zhong, X. Huang, W.-Y. Wong, H. Wu, L. Chen, S. Su and Y. Cao, *Adv. Mater.*, 2011, **23,** 4636-4643.
31 H.-C. Chen, Y.-H. Chen, C.-C. Liu, Y.-C. Chien, S.-W. Chou and P.-T. Chou, *Chem. Mater.*, 2012, **24,** 4766-4772.
32 Z. He, C. Zhong, S. Su, M. Xu, H. Wu and Y. Cao, *Nat. Photonics*, 2012, **6,** 591-595.
33 T. Yang, M. Wang, C. Duan, X. Hu, L. Huang, J. Peng, F. Huang and X. Gong, *Energy Environ. Sci.*, 2012, **5,** 8208-8214.
34 M. Zhang, X. Guo, S. Zhang, and J. Hou, *Adv. Mater.*, 2014, **26**, 1118–1123.

35 F. C. Krebs and K. Norrman, *Progr. Photovolt.: Res. Appl.*, 2007, **15,** 697-712.
36 M. Jørgensen, K. Norman and F. C. Krebs, *Sol. Energy Mater. Sol. Cells*, 2008, **92,** 686-714.
37 M. P. de Jong, L. J. van Ijzendoorn and M. J. A. de Voigt, *Appl. Phys. Lett.*, 2000, **77,** 2255-2257.
38 R. Pacios, A. J. Chatten, K. Kawano, J. R. Durrant, D. D. C. Bradley and J. Nelson, *Adv. Funct. Mater.*, 2006, **16,** 2117-2126.
39 H. Pan, Y. Li, Y. Wu, P. Liu, B. S. Ong, S. Zhu and G. Xu, *Chem. Mater.*, 2006, **18,** 3237-3241
40 H. Pan, Y. Wu, Y. Li, P. Liu, B. S. Ong, S. Zhu and G. Xu, *Adv. Funct. Mater.*, 2007, **17,** 3574-3579.
41 I. McCulloch, R. S. Ashraf, L. Biniek, H. Bronstein, C. Combe, J. E. Donaghey, D. I. James, C. B. Nielsen, B. C. Schroeder and W. Zhang, *Acc. Chem. Res.*, 2012, **45,** 714-722.
42 C. J. Brabec, A. Cravino, D. Meissner, N. S. Sariciftci, T. Fromherz, M. T. Rispens, L. Sanchez and J. C. Hummelen, *Adv. Funct. Mater.*, 2001, **11,** 374-380.
43 M. C. Scharber, D. Mühlbacher, M. Koppe, P. Denk, C. Waldauf, A. J. Heeger and C. J. Brabec, *Adv. Mater.*, 2006, **18,** 789-794.
44 R. Duan, L. Ye, X. Guo, Y. Huang, P. Wang, S. Zhang, J. Zhang, L. Huo, and J. Hou, *Macromolecules*, 2012, **45**, 3032−3038.
45 I. A. Howard, R. Mauer, M. Meister and F. Laquai, *J. Am. Chem. Soc.*, 2010, **132,** 14866-14876.
46 J. Peet, J. Y. Kim, N. E. Coates, W. L. Ma, D. Moses, A. J. Heeger and G. C. Bazan, *Nat. Mater.*, 2007, **6,** 497-500.
47 J. K. Lee, W. L. Ma, C. J. Brabec, J. Yuen, J. S. Moon, J. Y. Kim, K. Lee, G. C. Bazan and A. J. Heeger, *J. Am. Chem. Soc.*, 2008, **130,** 3619-3623.
48 D. Di Nuzzo, A. Aguirre, M. Shahid, V. S. Gevaerts, S. C. J. Meskers and R. A. J. Janssen, *Adv. Mater.*, 2010, **22,** 4321-4324.
49 T. Salim, L. H. Wong, B. Bräuer, R. Kukreja, Y. L. Foo, Z. Bao and Y. M. Lam, *J. Mater. Chem.*, 2011, **21,** 242-250.
50 J. J. M. Halls, K. Pichler, R. H. Friend, S. C. Moratti and A. B. Holmes, *Appl. Phys. Lett.*, 1996, **68,** 3120-3122.
51 M. Dutta, S. Mridha and D. Basak, *Appl. Surf. Sci.*, 2008, **254,** 2743-2747.
52 C.-I Wu, Y. Hirose, H. Sirringhaus and A. Kahn, *Chem. Phys. Lett.*, 1997, **272,** 43-47.
53 C.-I Wu and A. Kahn, *Appl. Phys. Lett.*, 1999, **74,** 546-548.
54 V. D. Mihailetchi, L. J. A. Koster, P. W. M. Blom, C. Melzer, B. de Boer, J. K. J. van Duren and R. A. J. Janssen, *Adv. Funct. Mater.*, 2005, **15,** 795-801.
55 V. D. Mihailetchi, H. Xie, B. de Boer, L. J. A. Koster and P. W. M. Blom, *A2dv. Funct. Mater.*, 2006, **16,** 699-708.

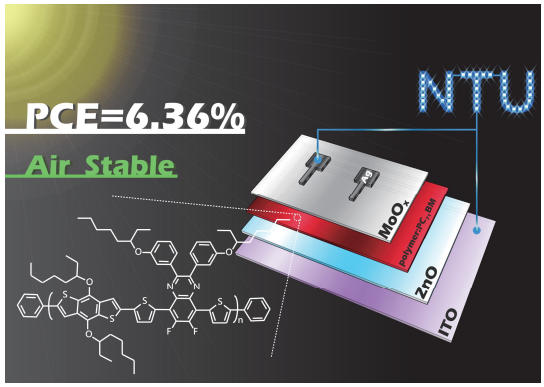

A newly medium bandgap PBDTQEH polymer solar cell with PCE of 6.36% was reported and demonstrated an outstanding long-term air stability.